SDSimPoint: Shallow–Deep Similarity Learning for Few-Shot Point Cloud Semantic Segmentation

Jiahui Wang, Haiyue Zhu, *Member, IEEE*, Haoren Guo, Abdullah Al Mamun, Cheng Xiang, *Member, IEEE*, Clarence W. de Silva, *Life Fellow, IEEE*, and Tong Heng Lee

***Abstract*— Three-dimensional point cloud semantic segmentation is a fundamental task in computer vision. As the fully supervised approaches suffer from the generalization issue with limited data, few-shot point cloud segmentation models have been proposed to address the flexible adaptation. Nevertheless, due to the class-agnostic nature of the few-shot pretraining, its pretrained feature extractor is hard to capture the class-related intrinsic and abstract information. Therefore, we introduce the new concept of shallow and deep similarities and propose a shallow–deep similarity learning network (SDSimPoint) that aims to learn both shallow (superficial geometry, color, etc.) and deep similarities (intrinsic context and semantics, etc.) between the support and query samples, thereby boosting the performance. Moreover, we design a beyond-episode attention module (BEAM) to enlarge the region of the attention mechanism from a single episode to the entire dataset by utilizing the memory units, which enhances the extraction ability to better capture the shallow and deep similarities. Furthermore, our distance metric function is learnable in the proposed framework, which can better adapt to complex data distributions. Our proposed SDSimPoint consistently demonstrates substantial improvements compared to baseline approaches across various datasets in diverse few-shot point cloud semantic segmentation settings.**

***Index Terms*— Few-shot learning, point cloud, self-supervised pretraining, semantic segmentation, similarity learning.**

I. Introduction

THE learning and development of 3-D scenes is becoming increasingly important in the modern world. This advancement in 3-D scene learning is beneficial for a variety of applications, including robotics, autonomous vehicles, manufacturing, and other industries with various data formats such as point cloud and mesh [1]. Among these applications that benefit from 3-D scene learning, the task of semantic segmentation of point cloud data is a critical and essential one. The goal of point cloud semantic segmentation is to recognize and classify the semantic properties and characteristics of each data point that makes up the 3-D object or scene. With the recent developments in deep learning with neural networks, several fully supervised models have been proposed for point cloud semantic segmentation [2], [3], [4], [5]. For instance, PointNet [2] is the first work that processes point clouds with multilayer perceptron (MLP), which uses a symmetric function to extract the features from the point clouds. The LGGCM [5] adopted a local spatial attention convolution with a smooth module and a global spatial attention module with a gated unit for effective receptive fields with long-range contexts at a relatively low computational cost. Generally, those fully supervised point cloud semantic segmentation methods are delicately designed to capture the discriminative features based on the trained classes. Therefore, the performance of a fully supervised method suffers from poor generalization ability with serious class bias if the training dataset is insufficient and monotonous. As a result, for those point cloud semantic segmentation applications with data scarcity or task liability, the fully supervised approaches are hard to meet the practical requirements.

To address the aforementioned issue, previous research adopts the few-shot learning to enable the model to adapt to novel classes effectively with a few samples [6], [7], [8], [9]. However, for the few-shot 3-D point cloud semantic segmentation tasks, we hardly can use a well-trained backbone with abundant class numbers to conduct "open-vocabulary" inference due to the scale of the available data in the real world. Some researchers tried to achieve this task by pretraining a backbone in a relatively small dataset, learning the per-point feature, and then measuring the query-support distance for prediction [10], [11], [12], [13]. This paradigm is effective but still suffers from a data scale for supervised pretraining.

Wang et al. [14] used a self-supervised pretraining to enlarge the data scale, but the learned features are improvable in some perspective. The features extracted by such a backbone can be competent in many scenarios as they contain superficial information for effective similarity measures such as the geometry, color, and position properties between the objects, which we term as shallow similarity. However, due to the limitation on quality and scalability of the 3-D datasets, the pretrained 3-D feature extractor might not be able to understand universal

Received 9 April 2024; revised 24 October 2024; accepted 10 February 2025. Date of publication 24 March 2025; date of current version 4 June 2025. This work was supported in part by the National University of Singapore through the College of Design and Engineering Industry-Focused Ring-Fenced Ph.D. Scholarship Program and in part by A*STAR through the National Research Foundation (NRF) "Centre for Advanced Robotics Technology Innovation (CARTIN)" Program. *(Corresponding author: Haiyue Zhu.)*

Jiahui Wang, Haoren Guo, Abdullah Al Mamun, Cheng Xiang, and Tong Heng Lee are with the College of Design and Engineering, Electrical and Computer Engineering, National University of Singapore, Singapore 117582.

Haiyue Zhu is with Singapore Institute of Manufacturing Technology (SIMTech), Agency for Science, Technology and Research (A*STAR), Singapore 138634 (e-mail: zhu_haiyue@simtech.a-star.edu.sg).

Clarence W. de Silva is with the Department of Mechanical Engineering, The University of British Columbia, Vancouver, BC V6T 1Z4, Canada (e-mail: desilva@mech.ubc.ca).

Digital Object Identifier 10.1109/TNNLS.2025.3543620

high-level features, especially when facing a complex scene. We argue that such shallow similarity using superficial information directly extracted by the backbone makes it difficult to capture the deep relationship between the objects, which relies on intrinsic information such as semantics, context, and rationality, especially for a self-supervised pretrained backbone. For instance, distinguishing sofas from different scenes with diverse colors and shapes may need such deep similarity for precise predictions, and the shallow similarity based on superficial information is incapable of capturing the intrinsic feature due to the diversities and inconsistency of appearances and contexts. Essentially, this is because the backbone extractor employed in few-shot models is pretrained in a task-agnostic manner, which is different from the fully supervised scenarios. As a result, such models only consider shallow similarity, which generally leads to the unsatisfied performance of complex objects and scenes. Inspired by this finding, we propose SDSimPoint in this work, which takes both the shallow and deep similarities into account simultaneously to enhance the prediction performance for complex scenarios.

Moreover, to better capture the effective similarity between query and support samples, the self-attention (SA) mechanism is commonly used in many few-shot learners to enhance the learning of context information [10], [15], [16]. In a traditional fully supervised manner [10], the SA unit looks through the samples in a batch that contains varied samples with diverse information. As a result, a larger batch size encourages SA to capture the global dependencies better and learn more robust attention patterns, thus improving performance. However, when it comes to the episodic training in the few-shot learning, the horizon of SA is constrained within one episode in N-way K-shot. As N and K are small, they limit the exposure of SA to diverse examples and may negatively prioritize attention to local dependencies. Motivated by this finding, we propose a beyond-episode attention module (BEAM) for the few-shot learning in episode training, which facilitates SAs to capture the long-range global attention information across episodes. The main contributions of this work are summarized as follows.

1) We develop a new categorization of shallow and deep similarities for few-shot learning and propose SDSimPoint, a shallow–deep similarity learning framework for point cloud semantic segmentation.
2) A shallow similarity module (SSM) is designed to learn the superficial similarity, and a deep similarity module (DSM) is proposed to capture the intrinsic similarity through deep query-prototype interaction and fusion.
3) A BEAM is introduced that enables the attention mechanism to break the episode constraint and capture the long-range global information.

II. Related Works

A. Few-Shot Learning

The mainstream few-shot learning methods can be broadly categorized into four categories, i.e., data-based [17], [18], model-based [7], [19], [20], [21], optimization-based [22], [23], [24], and metric-based [7], [8], [9], [25], [26] methods. Data-based methods, exemplified by FlipDA [27], aim to generate additional training data or features through augmentation or synthesis to improve the few-shot performance. Model-based methods leverage some specific model architectures, such as recurrent and memory-enhanced networks, to enable the memorization of samples even with minimal exposure. In optimization-based methods, MAML [24] focuses on finding optimal initial states or parameter settings during the training, which enables the model to perform well on new tasks by updating with a small number of samples. He et al. [28] proposed a registration module that enables the model to learn robust representation with few samples. For metric-based methods, the central concept is to learn a good feature embedding space for acquiring similarity measure metrics, which can effectively capture the correspondence between support and query samples. ProtoNet [9] aims to generate the prototype for each class, which will be used as the anchor to calculate the similarity metric and predict the classes for queries. DFR [29] focuses on extracting the class-discriminative features from the variations distracting the metric learning, thus improving few-shot classification performance. TRSN [30] divides the few-shot learning task into three subparts, explicitly models the task-related saliency features, and makes use of them for prediction. BSSD [31] replaces global feature vectors with enhanced local feature maps that are more consistent between seen and unseen classes to mitigate the data-scarcity issue, and then uses Sinkhorn distance to measure the similarity. Some works [8] use graph-based techniques to build accurate correspondence for better metric learning interpretability. Thanks to its simplicity and effectiveness, the metric-based methods have been widely used in recent few-shot learning research.

B. Point Cloud Semantic Segmentation

The pioneering work, PointNet [2], shows the potential of adopting deep learning in point cloud semantic segmentation. More models are proposed in different perspectives [4], [5], [32], [33], [34], [35], [36], [37]. They can be divided into the following categories: graph-based [5], [32], MLP-based [4], [33], [34], and transformer-based [35], [36], [37] methods. SPG [32] adopts a method to extract super points from a large point cloud scene and construct a correspondence graph for contextual information learning. MLP-based methods, taking PointNeXt [34] as an example, use a set of improved training and sampling strategies and design residual bottleneck layers as well as separable MLPs to facilitate efficient and impactful model up-scaling. PointTransformer [35] first imports transformer into a 3-D point cloud. It treats points of the downsampled scene as the token of transformer blocks with a designed vector SA to effectively learn the information of 3-D point clouds. Recently, PointTransformerV3 [37] represents a notable advancement over the original PointTransformer. This improvement primarily involves substituting the meticulous neighbor search with a more efficient serialized neighbor mapping technique applied to point clouds structured according to distinct patterns.

In the realm of few-shot point cloud semantic segmentation, several innovative approaches have emerged [10], [11], [12],

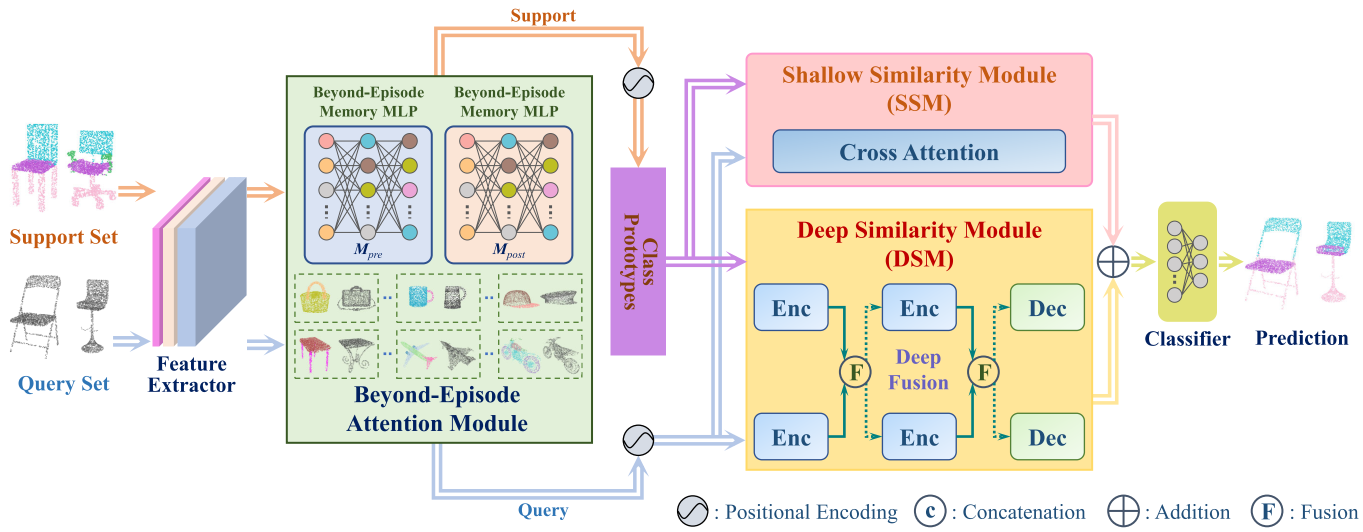

Fig. 1. Architecture of SDSimPoint. We introduce the new categorization of shallow and deep similarities for few-shot point cloud segmentation. The "shallow" refers to superficial information that can be well-captured by the pretrained extraction and attention module, while the "deep" refers to class-related intrinsic characteristics that are hard to capture due to class-agnostic pretraining. Therefore, we design the SSM and DSM to separately capture the shallow and deep similarities, where a query-prototype deep-fusion mechanism is introduced in DSM. Moreover, a BEAM module is introduced for effective attention to break the episode constraint and capture the long-range global information.

[13], [38], [39], [40], [41]. AttMPTI [10] pioneered the use of label propagation to connect prototypes and query points using pretrained feature extraction. PEFC [42] employs specialized components for prototype set expansion and adjustment based on query characteristics. PAPFZS3D [11] introduces a framework that simultaneously refines both prototypes and query features. SCAT [41] implements a class-specific, multilayered attention transformer to establish detailed support-query feature associations. COSeg [13] utilizes a correlation memory-based network to uncover inherent query-prototype relationships. Seg-PN [40] offers a computationally efficient solution using a nonparametric encoder and correlation-driven interactions between support and query for pointwise classification.

III. Methodology

A. Problem Formulation

To facilitate the few-shot learning and inference pipeline, the few-shot point cloud semantic segmentation to address in this work is formulated as an N-way K-shot problem [10], [14], [43], [44]. Given a support set $\mathcal{S} = \{(\boldsymbol{P}_s^{n,k}, \boldsymbol{Y}_s^{n,k})_{k=1}^{K}\}_{n=1}^{N}$, where N is the number of classes, each class consists of K support point cloud samples $\boldsymbol{P}_s$ with the corresponding labels $\boldsymbol{Y}_s$. The query set is defined as $\mathcal{Q} = (\boldsymbol{P}_q, \boldsymbol{Y}_q)$ accordingly, where $\boldsymbol{Y}_q$ is the ground truth and not available during the training. The objective of this work is to design the network architecture $\mathcal{N}_\theta(\cdot)$ and obtain its optimal parameter θ^*

$$\begin{aligned} \hat{\boldsymbol{Y}}_q &= \mathcal{N}_\theta(\boldsymbol{P}_q|\mathcal{S}) \\ \theta^* &= \underset{\theta}{\operatorname{argmin}} \sum_{\boldsymbol{P}_q \in \mathcal{Q}} \mathcal{L}(\boldsymbol{Y}_q, \hat{\boldsymbol{Y}}_q) \end{aligned} \tag{1}$$

where $\mathcal{L}$ is the loss function. By minimizing the loss, the information entropy between the prediction and the ground truth is optimized, which ensures a promising result. In this work, the episodic learning paradigm [10], [14], [43], [44] is employed for the few-shot training.

B. Overview

Fig. 1 illustrates the overall architecture of the proposed approach. First, a pretrained backbone is employed in the pipeline to perform the basic feature extraction, which is self-supervised from the public point cloud datasets [14]. To better capture the relationships across spatial locations in the feature embedding, the attention module is utilized to improve the similarity correspondence. Uniquely, the proposed BEAM in this work extends the attention horizon beyond the episode, which employs a memory unit across the episodes to enhance the long-range dependencies. After that, using the feature embedding from BEAM, the class prototypes are generated from the training samples in the support set, which will be used to measure the similarity with the query samples.

In this work, we propose shallow–deep similarity learning to effectively capture both the superficial and intrinsic information to build correspondence. Fig. 2 depicts the shallow similarity and deep similarity, respectively. The query feature embedding and the class prototypes from the support set are fed into both the SSM and the DSM concurrently to grab the shallow and deep similarities. The SSM takes advantage of the direct feature embedding for similarity measure, which is responsible for capturing superficial similarities such as geometry, color, and position. The pretrained feature extractor employed in few-shot models is trained in a task-agnostic manner, which is not as capable as those fully supervised models to capture the class-specific high-level semantic information. Therefore, we propose the DSM with additional encoder–decoder structures, which are shown in Fig. 3 to make deep-fusion interactions between the query embedding and class prototypes. Finally, a learnable point classifier takes both the shallow and deep similarity feature maps as input

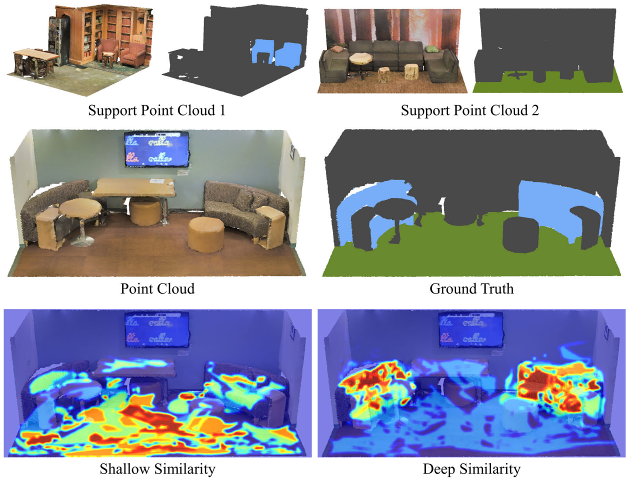

Fig. 2. Similarity visualization between query and support samples: the shallow similarity focuses more on the objects sharing similar geometry or color, while the deep similarity is more relative to the objects with different shapes and colors but sharing similar semantic information. The segmentation performance can be improved by combining both the shallow and deep similarities.

and makes the final predictions for all points with the highest similarity classes.

C. Beyond-Episode Attention Module

SA mechanism [45], [46] is widely used for capturing contextual information in many computer vision tasks. However, we argue that for the few-shot point cloud semantic segmentation, the attention horizon of SA is constrained within the current episode. This is very different from the fully supervised scenarios, which can look through the samples from all randomly formed batches across the whole abundant and diverse dataset. Such a constraint limits the understanding and utilization of the information in the scale of the whole training data. Furthermore, unlike the images, point clouds are hard to split into patches for SA due to their unordered nature. As a result, the SA for a point cloud with M points exhibits a time complexity of $\mathcal{O}(M^2)$, where M is normally a large number and thus requires tremendous computation resources.

Inspired by [47], the proposed BEAM adopts the concept of external attention and extends it into a two-stage hierarchical structure with beyond-episode awareness. Our BEAM consists of two memory units $\mathcal{M}_{\text{pre}}(\cdot)$ and $\mathcal{M}_{\text{post}}(\cdot)$, which is realized by the simple MLP. Specifically, consider one point cloud $\boldsymbol{P} \in \{\mathcal{S}_i, \mathcal{Q}_i\}$ for ith episode, the prememory unit $\mathcal{M}_{\text{pre}}(\cdot)$ processes the concatenation of backbone feature and position information

$$\boldsymbol{F}_i^{\text{pre}} = \mathcal{M}_{\text{pre}}\left(\left[\mathcal{B}(\boldsymbol{P}); \text{pos}(\boldsymbol{P})\right] \middle| \boldsymbol{\theta}_i^{\text{pre}}\right) \tag{2}$$

where $\mathcal{B}(\cdot)$ is the backbone extractor, pos$(\cdot)$ denotes the point xyz positions for $\boldsymbol{P}$, and $\boldsymbol{\theta}_i^{\text{pre}}$ refers to the weights for $\mathcal{M}_{\text{pre}}$ in the ith episode. To enhance the memory unit with better beyond-episode awareness, we adopt a simple yet efficient exponential moving average (EMA) rule for updating the weights, i.e.,

$$\widetilde{\boldsymbol{\theta}}_i^{\text{pre}} = \alpha\boldsymbol{\theta}_i^{\text{pre}} + (1-\alpha)\widetilde{\boldsymbol{\theta}}_{i-1}^{\text{pre}} \tag{3}$$

where α is a decay hyperparameter. During training, the $\boldsymbol{\theta}_i^{\text{pre}}$ is updated with the gradient descent. The feature from the prememory unit is then fed into a normalization layer, and the postmemory unit $\mathcal{M}_{\text{post}}(\cdot)$ takes the normalized feature as the input to generate the postattention feature

$$\boldsymbol{F}_i^{\text{post}} = \mathcal{M}_{\text{post}}\left(\text{Norm}\left(\boldsymbol{F}_i^{\text{pre}}\right) \middle| \boldsymbol{\theta}_i^{\text{post}}\right) \tag{4}$$

where Norm$(\cdot)$ denotes the normalization operation, and the same EMA rules apply for $\mathcal{M}_{\text{post}}(\cdot)$. Consequently, in one episode, for both support and query samples, the output feature is the concatenated feature from BEAM extraction and backbone extraction, together with the positional embedding, i.e.,

$$\boldsymbol{F}_t^{\text{beam}} = \text{Concat}\left(\mathcal{B}(\boldsymbol{P}_t); \boldsymbol{F}_t^{\text{post}}\right) + \mathbf{PE} \tag{5}$$

where $t \in \{q, s\}$ denotes the respective query or support features, Concat$(\cdot)$ is the concatenation operation, and **PE** represents the common sinusoidal positional embedding. $\boldsymbol{F}_t^{\text{beam}}$ will be used for both SSM and DSM to measure the similarity in the next stages.

D. Shallow–Deep Similarity

We propose the shallow–deep similarity learning for few-shot point cloud segmentation. As common sense, objects within the same category are supposed to exhibit more commonalities in color appearance and geometrical shape. Therefore, a native solution for few-shot point cloud segmentation is to leverage such characteristics to identify the analogous points/objects from the query point cloud to those support point clouds. Such superficial commonalities in color, geometry, etc., can be well-captured by the pretrained feature extractor, and many few-shot segmentors [10], [48], [49] have already adopted this approach as an intuitive-yet-efficient solution. In this work, we term this native superficial similarity as the "shallow similarity" to differentiate from the concept of "deep similarity," which conveys high-level intrinsic and abstract information such as semantics and context. It is worth noting that shallow similarity is an effective and complementary measure as it emphasizes the geometrical shape, color, and surface characteristics, which convey discriminative information at diverse frequency bands. Consequently, we propose an SSM to grasp such a shallow similarity.

However, we argue that due to the supervision constraints of the few-shot learning, a pretrained few-shot feature extractor is good for capturing the shallow and superficial similarities between the query and support samples while being weak in capturing the deep and intrinsic similarities. It is worth noting that, for common fully supervised learning, the concept of separation between shallow and deep similarities is not valid. This is because their feature extractors, either CNN or attentions, are supposed to handle both the shallow and deep similarities concurrently through the class-specific and sample-abundant fully supervised training. Essentially, the deep similarity is the intrinsic characteristics related to the specific class, which includes the high-level abstract semantics and context relationship with the background, etc. For a few-shot segmentation scene, both shallow and deep similarities will occur, but the attention paid to them should be

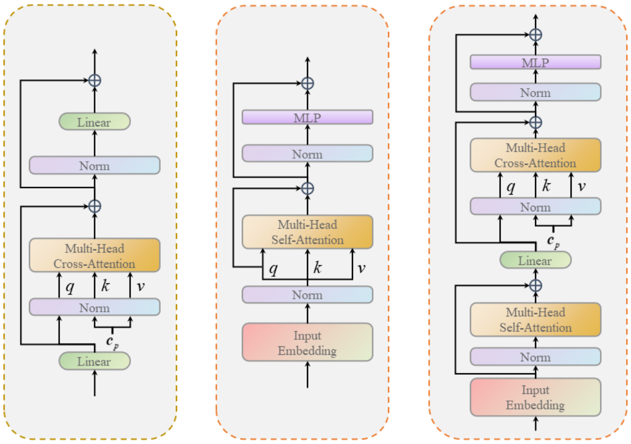
Linear
Norm
Multi-Head Cross-Attention
q
k
v
Norm
c_p
Linear
MLP
Norm
Multi-Head Self-Attention
q
k
v
Norm
Input Embedding
MLP
Norm
Multi-Head Cross-Attention
q
k
v
Norm
c_p
Linear
Multi-Head Self-Attention
Norm
Input Embedding

(a) (b) (c)

Fig. 3. Architectures of SSM and DSM. The SSM only has one cross-attention module to learn the superficial similarity, while each DSM block consists of an encoder and a decoder. The encoder in the DSM excavates deeper semantic features for queries and prototypes with SA and then sends such "high-level" information to the fusion process. The decoder in the DSM receives the fused feature and measures the deep similarity between query and prototypes with self- and cross-attentions. (a) SSM. (b) Encoder of DSM. (c) Decoder of DSM.

adaptive due to different scenarios. For example, a scene with fewer objects and a straightforward layout can be segmented well based on shallow similarity. Segmentation for complex scenes, on the contrary, should involve deeper similarity for a more accurate result as they rely on high-level semantic-related information, which is more robust and representative. However, the pretraining of a few-shot feature extractor is not possible to have class-specific training as it aims to handle novel classes, which are unknown at the pretraining stage. Although we can fine-tune such a pretrained network in a class-specific manner to enhance the learning for the deep similarity between samples, the few-shot tasks usually lack sufficient samples even for such fine-tuning. Therefore, a more effective way is to capture the deep similarity in the adaptation stage through some delicately designed mechanisms. To this end, we propose a DSM that uses a query-prototype deep-fusion mechanism and cascaded attention blocks to capture the deep similarity.

E. Shallow Similarity Module

In this work, our SSM is simply realized based on the multihead cross-attention (MHCA) module, where its architecture is shown in Fig. 3(a). For both SSM and DSM, the similarity is measured between the query sample features $\boldsymbol{F}_q^{\text{beam}}$ and the class prototypes $\boldsymbol{c}_p$ generated from the support samples. The class prototype is the mean of the extracted support feature $\boldsymbol{F}_s^{\text{beam}}$ for points belonging to its respective class, which describes the distribution of class characteristics in the feature space. Next, both $\boldsymbol{F}_q^{\text{beam}}$ and $\boldsymbol{c}_p$ are projected into a latent space with simple linear layers and normalization, and the MHCA block is used to capture the cross-attention for similarity measure, denoted as

$$\boldsymbol{F}_q^{\text{ca}} = \text{MHCA}\left(\boldsymbol{F}_q^{\text{beam}}, \boldsymbol{c}_p, \boldsymbol{c}_p\right) \tag{6}$$

where MHCA$(\cdot)$ takes $\boldsymbol{F}_q^{\text{beam}}$ as query and $\boldsymbol{c}_p$ as key and value in the cross-attention. Lastly, we employ the residual structure to get the final output for SSM

$$\boldsymbol{F}_q^{\text{ssm}} = \mathcal{R}\text{es}\left(\boldsymbol{F}_q^{\text{ca}} + \boldsymbol{F}_q^{\text{beam}}\right) \tag{7}$$

where $\mathcal{R}\text{es}(\cdot)$ denotes the residual operation, i.e., $\mathcal{R}\text{es}(\boldsymbol{F}) = \boldsymbol{F} + \text{Linear}(\text{Norm}(\boldsymbol{F}))$ as indicated in Fig. 3(a).

F. Deep Similarity Module

Our intention for DSM is to facilitate more "interaction" between the query feature and support prototypes so that the intrinsic similarity can be measured through deep fusion. Such fusion technique has already been proved in many works such as GLIP [50], [51] and FIBER [25], [52]. Different from SSM, which has no fusion process, this interaction enables the DSM gradually to learn different information rather than focus on dominant shallow similarity. The cascaded attention blocks help the DSM to utilize hierarchical features that facilitate the learning of deeper similarity. With these designs, the query feature not only holds basic representations but also incorporates details about the pointwise assignment, where the query point is classified into the group that shows the highest similarity to its corresponding prototype.

The DSM consists of M encoders and N decoders for both query and prototypes. The structures of the encoder and decoder are illustrated in Fig. 3(b) and (c), respectively. Let $\text{Enc}_{\text{dsm}}^m(\cdot)$ and $\text{Dec}_{\text{dsm}}^n(\cdot)$ denote the mth encoder and nth decoder, respectively, $m \in [0, M-1]$, and $n \in [0, N-1]$. The DSM takes the query sample features $\boldsymbol{F}_q^{\text{beam}}$ and the class prototypes $\boldsymbol{c}_p$ as the initial inputs, the query, and prototype features are encoded for fusion as

$$\boldsymbol{F}_t^{m+1} = \text{Enc}_{\text{dsm}}^m\left(\boldsymbol{F}_t^m\right) \tag{8}$$

where $t \in \{q, p\}$ denotes the query and class prototype, and $\boldsymbol{F}_q^0 = \boldsymbol{F}_q^{\text{beam}}$ and $\boldsymbol{F}_p^0 = \boldsymbol{c}_p$. After every encoder, the query and prototype features are first projected by a learnable matrix $\boldsymbol{W}_1 \in \mathbb{R}^{C\times C}$, and the fusion map $\boldsymbol{U}_m$ is calculated as

$$\boldsymbol{U}_m = \text{SoftMax}\left(\frac{\left(\boldsymbol{F}_q^m \otimes \boldsymbol{W}_1\right) \otimes \left(\boldsymbol{F}_p^m \otimes \boldsymbol{W}_1\right)^\top}{\sqrt{C}}\right) \tag{9}$$

where $\otimes$ represents the matrix multiplication. Next, the fused features are obtained by multiplication with another learnable matrix $\boldsymbol{W}_2$

$$\begin{aligned}\tilde{\boldsymbol{F}}_q^m &= \boldsymbol{U}_m \otimes \left(\boldsymbol{F}_p^m \otimes \boldsymbol{W}_2\right)\\ \tilde{\boldsymbol{F}}_p^m &= \boldsymbol{U}_m^\top \otimes \left(\boldsymbol{F}_q^m \otimes \boldsymbol{W}_2\right)\end{aligned} \tag{10}$$

where $\tilde{\boldsymbol{F}}_q^m$ and $\tilde{\boldsymbol{F}}_p^m$ denote the fused features, respectively, where these will be used as the inputs for next encoders.

In the decoding stage, the query and prototype features are decoded separately using $\text{Dec}_{\text{dsm}}^n(\cdot)$. The last decoded query feature will be used as the DSM output, which is denoted as $\boldsymbol{F}_q^{\text{dsm}}$. Finally, by fusing the SSM and DSM extracted similarity features, the prediction can be made by

$$\boldsymbol{Y}_q = \text{CLS}\left(\boldsymbol{F}_q^{\text{ssm}} + \boldsymbol{F}_q^{\text{dsm}}\right) \tag{11}$$

where CLS$(\cdot)$ is a learnable MLP-based classifier. The loss functions for training and pretraining are discussed in Section IV-B.

IV. Experiment

A. Data Preparation

The S3DIS dataset [56] and the ScanNet dataset [57] are selected as benchmark datasets because they are widely recognized in 3-D semantic segmentation tasks. The S3DIS dataset consists of five regions, comprising a total of 271 rooms, with each area containing multiple objects in 13 semantic categories, such as sofas, chairs, and tables, among others. However, processing entire rooms is challenging due to their substantial size. Therefore, we follow the approach outlined in [2] to divide rooms into blocks, with each block containing approximately 20 000 points. The ScanNet dataset [57] is more complex, with 1513 regions and 21 semantic classes. Similarly, we segment this dataset into blocks, with each block containing about 8000 points. Each point in the datasets mentioned above is represented by a 9-D vector, which includes coordinate vectors: x, y, z; color vectors: r, g, b; and normed vectors n_x, n_y, n_z. During the training stage, we randomly sample 2048 points for each block. Following the approach in [10] and [38], we divide each dataset into two nonoverlapping subsets named S^0 and S^1; one of them is adopted only in testing, and the other is used for the pretraining and training.

B. Implementation Details

For the backbone (feature extractor), we adopt DGCNN [58] as previous methods [10], [11] and pretrain it for 200 epochs to ensure the fairness in subsequent comparison. During the pretraining stage, we follow the paradigm in [14] that input two alternate views, denoted as $\boldsymbol{P}, \boldsymbol{P}' \in \mathbb{R}^{M\times 9}$, into the feature extractor $\mathcal{B}$ along with a classification head to obtain two segmentation outputs, $\boldsymbol{O}, \boldsymbol{O}' \in \mathbb{R}^{\mathbb{M}\times\mathbb{N}}$, where N_c represents the total number of classes in the pretraining dataset. The contrastive loss is then formulated to bring similar points in $\boldsymbol{O}$ and $\boldsymbol{O}'$ closer together while pushing other points away in the feature space

$$\mathcal{L}_{\text{con}} = \mathop{\mathbb{E}}_{o_i \in \boldsymbol{O}} \left[-\log \left(\frac{e^{o_i (o_i')^\top}}{\sum_{j=1}^{M} e^{o_i \left(o_j'\right)^\top}} \right) \middle| o_j' \in \boldsymbol{O}' \right] \tag{12}$$

where o_i and o_i' represent the ith point predictions in $\boldsymbol{O}$ and $\boldsymbol{O}'$, respectively. The learning rate is set to 0.001, and the value of k in the k-NN algorithm is set to 20. Our batch size is 16, designed for running the model on a single GPU, and a weight decay ratio of 0.01 is employed to prevent severe overfitting.

For the dynamic augmentor, the Chamfer distance loss [59] is adopted to enhance the augmentation performance

$$\mathcal{L}_{\text{CD}} = \lambda \left\{ \frac{1}{|\boldsymbol{P}|} \sum_{x \in \boldsymbol{P}} \min_{y \in \boldsymbol{P}'} \|x - y\|_2^2 + \frac{1}{|\boldsymbol{P}'|} \sum_{y \in \boldsymbol{P}'} \min_{x \in \boldsymbol{P}} \|x - y\|_2^2 \right\} \tag{13}$$

where x and y denote the points belonging to $\boldsymbol{P}$ and $\boldsymbol{P}'$, respectively. We update their parameters along with the feature extractor for 60 epochs, after which we fix the augmentor and solely pretrain the feature extractor. The coefficient λ for $\mathcal{L}_{\text{CD}}$ is set to -0.01. Given these settings, we utilize the Adam optimizer with a learning rate decay ratio of 0.5 and a decay step of 50 epochs.

In the training stage, the ground truth of the query set, $\boldsymbol{Y}_q$, and the prediction of our model, $\boldsymbol{Y}_q'$, are used for the cross-entropy loss computation, which can be expressed as

$$\mathcal{L} = -\frac{1}{|\mathcal{Q}|}\frac{1}{M} \sum_{i=1}^{|\mathcal{Q}|} \sum_{j=1}^{M} \sum_{n=1}^{N} \mathbb{1}\{\boldsymbol{Y}_q[i, j] = n\} \log\left(\hat{\boldsymbol{Y}}_q[i, j, n]\right) \tag{14}$$

where the one-hot prediction $\hat{\boldsymbol{Y}}_q = \text{SoftMax}(\boldsymbol{Y}_q')$ is the output of our model. We also update the parameters in the feature extractor with a small learning rate of 0.00005. The general learning rate for the SSM and DSM blocks is 0.001. For the BEAM module, we set the number of attention heads to 8 and the hyperparameter α to 0.99. To balance computation efficiency and performance, we configure the number of encoders and decoders in DSM to 3. The number of heads in all cross-attention units is set to 2, while for SA units, it is set to 4.

Each class has 100 prototype numbers. The dropout rate in DSM and SSM is set to 0, and LayerNorm [60] is applied to all normalization layers. The classifier is an MLP with the LeakyReLu activation function, with a threshold set to 0.2. To avoid overfitting, we additionally add a dropout layer with a 0.25 rate to the classifier. We train our model on an NVIDIA RTX 3090 GPU for 45 000 iterations, with a learning rate decay ratio of 0.5 and decay steps every 5000 iterations. During training, we conduct the validation process every 2000 iterations for efficiency. We evaluate the performance of our model using the mean intersection over union (m-IoU) [10] as the metric. The model with the best performance on the validation set and trained for more than 10 000 iterations is saved for subsequent evaluation. For testing, we select 100 unseen episodes and then add Gaussian noises to simulate practical disturbance.

C. Benchmark and Result Comparison

The experiments are conducted to benchmark the performance from various aspects. As suggested by Newell and Deng [61], the pretraining can provide a better initialization for the feature extractor. This initialization is especially valuable for few-shot learning, as the limited availability of labeled data may not be sufficient to train the feature extractor effectively. Zhao et al. [10] pretrain the feature extractor with the same in-door scanning point cloud datasets as that in training; however, in practical application, the training dataset might not be large and complete enough for pretraining. Therefore, it is valuable to investigate the situation of using another dataset for pretraining while adopting our target dataset for training. According to [62], the two datasets used in [10] can be treated as in the same domain because they are both generated from real-world in-door scanning point clouds. Nonetheless, in some cases, it might be difficult to find an appropriate pretraining dataset within the same domain. Hence, we can explore datasets in other domains for pretraining, which is

TABLE I
S3DIS SEMANTIC SEGMENTATION RESULT USING M-IOU (UP,%) AND DICE COEFFICIENT (DOWN,%). S^i MEANS THAT THE TESTING DATASET IS THE iTH SPLIT

Method	2-way						3-way					
	1-shot			5-shot			1-shot			5-shot		
	S^0	S^1	mean	S^0	S^1	mean	S^0	S^1	mean	S^0	S^1	mean
FT [53]	36.34	38.79	37.57	56.49	56.99	56.74	30.05	32.19	31.12	46.88	47.57	47.23
ProtoNet [9]	48.39	49.98	49.19	57.34	63.22	60.28	40.81	45.07	42.94	49.05	53.42	51.24
AttProtoNet [9]	50.98	51.90	51.44	61.02	65.25	63.14	42.16	46.76	44.46	52.20	56.20	54.20
MPTI [10]	52.27	51.48	51.88	58.93	60.56	59.75	44.27	46.92	45.60	51.74	48.57	50.16
AttMPTI [10]	53.77	55.94	54.86	61.67	67.02	64.35	45.18	49.27	47.23	54.92	56.79	55.86
Aug-FT-P [38]	54.88	58.87	56.88	68.83	68.57	68.70	49.44	50.68	50.06	60.76	61.28	61.02
Aug-FT-A [38]	55.65	59.17	57.41	67.80	69.04	68.42	48.52	50.83	49.68	60.76	58.62	59.69
CWT [54]	52.14	57.86	55.00	61.64	66.48	64.06	-	-	-	-	-	-
BFG [55]	55.60	55.98	55.79	63.71	66.62	65.17	46.18	48.36	47.27	55.05	57.80	56.43
SCAT [41]	54.92	56.74	55.83	64.24	69.03	66.63	-	-	-	-	-	-
PEFC [42]	55.09	59.63	57.36	65.47	70.84	68.16	49.15	54.69	51.92	62.56	63.21	62.89
PAPFZS3D [11]	59.45	66.08	62.76	65.40	70.30	67.85	48.99	56.57	52.78	61.27	60.81	61.04
2CBR [12]	55.89	61.99	58.94	63.55	67.51	65.53	46.51	53.91	50.21	55.51	58.07	56.79
Seg-PN [40]	64.84	67.98	66.41	67.63	71.48	69.36	60.12	**63.22**	61.67	62.58	64.53	63.56
Ours	**68.73**	**70.61**	**69.67**	**72.12**	**72.72**	**72.42**	**62.28**	62.11	**62.19**	**65.17**	**66.10**	**65.64**
FT [53]	53.31	55.89	54.61	72.19	72.60	72.40	46.21	48.70	47.47	63.83	64.47	64.15
ProtoNet [9]	65.22	66.65	65.94	72.89	77.47	75.22	57.96	62.14	60.08	65.82	69.64	67.76
AttProtoNet [9]	67.53	68.33	67.93	75.79	78.97	77.41	59.31	63.72	61.55	68.59	71.96	70.30
MPTI [10]	68.65	67.97	68.32	74.16	75.44	74.80	61.37	63.87	62.64	68.20	65.38	66.81
AttMPTI [10]	69.94	71.75	70.85	76.29	80.25	78.31	62.24	66.01	64.16	70.90	72.44	71.68
Aug-FT-P [38]	70.87	74.11	72.51	81.54	81.35	81.45	66.17	67.27	66.72	75.59	75.99	75.79
Aug-FT-A [38]	71.51	74.35	72.94	80.81	81.68	81.25	65.34	67.40	66.38	75.59	73.91	74.76
CWT [54]	68.54	73.31	70.97	76.27	79.87	78.09	-	-	-	-	-	-
BFG [55]	71.47	71.78	71.62	77.83	79.97	78.91	63.18	65.19	64.20	71.01	73.26	72.15
SCAT [41]	70.90	72.40	71.66	78.23	81.68	79.97	-	-	-	-	-	-
PEFC [42]	71.04	74.71	72.90	79.13	82.93	81.07	65.91	70.71	68.35	76.97	77.46	77.22
PAPFZS3D [11]	74.57	79.58	77.12	79.08	82.56	80.85	65.76	72.26	69.09	75.98	75.63	75.81
2CBR [12]	71.70	76.54	74.17	77.71	80.60	79.18	63.49	70.05	66.85	71.39	73.47	72.44
Seg-PN [40]	78.67	80.94	79.81	80.69	83.37	81.91	75.09	**77.47**	76.29	76.98	78.44	77.72
Ours	**81.47**	**82.77**	**82.12**	**83.80**	**84.21**	**84.00**	**76.76**	76.63	**76.69**	**78.91**	**79.59**	**79.26**

significant for real-world applications. Figs. 4 and 5 illustrate our semantic segmentation result on S3DIS and ScanNet. The attMPTI [10] is adopted as the baseline; from the figures, it is evident that our method outperforms the baseline. Fig. 6 shows the visualized loss and accuracy curve during training and testing. The loss value gradually leveled out in training and testing. Looking at it in combination with the accuracy curve, the testing accuracy does not show a significant decline as the training loss decreases, and the testing loss remains stable. We can conclude that our model has not experienced significant overfitting under the mentioned experimental setup.

In light of these considerations, we undertake experiments in three distinct settings.

1) *Same-Domain Same Pretraining:* This paradigm aligns with the approach outlined in [10].
2) *Same-Domain Cross Pretraining:* In this scenario, the pretraining dataset differs from the training dataset, yet they both belong to the same domain.
3) *Cross-Domain Cross Pretraining:* Here, the pretraining dataset and the training dataset originate from distinct domains. This classification allows us to comprehensively explore the impact of different pretraining strategies on our experiments.

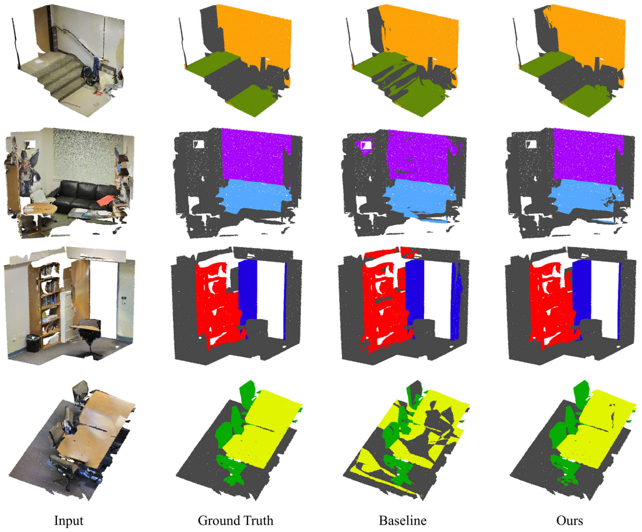

Fig. 4. Visualization of 2-way 1-shot segmentation result on *S3DIS* dataset. The involved classes are Wall and Floor (first row), Window and Sofa (second row), Bookcase and Door (third row), and Table and Chair (last row); the background points are denoted by dark gray points.

1) Same-Domain Same Pretraining: We conduct our SDSimPoint pipeline on S3DIS and ScanNet, respectively, where the pretraining and training datasets are the same as baseline [10]. The results of our method compared to the baselines are summarized in Tables I and II. With a larger shot number, which means more labeled samples, there are

TABLE II

SCANNET SEMANTIC SEGMENTATION RESULT USING M-IOU (UP,%) AND DICE COEFFICIENT (DOWN,%). S^i MEANS THAT THE TESTING DATASET IS THE iTH SPLIT

Method	2-way						3-way					
	1-shot			5-shot			1-shot			5-shot		
	S^0	S^1	mean	S^0	S^1	mean	S^0	S^1	mean	S^0	S^1	mean
FT [53]	31.55	28.94	30.25	42.71	37.24	39.98	23.99	19.10	21.55	34.93	28.10	31.52
ProtoNet [9]	33.92	30.95	32.44	45.34	42.01	43.68	28.47	26.13	27.30	37.36	34.98	36.17
AttProtoNet [9]	37.99	34.67	36.33	52.18	46.89	49.54	32.08	28.96	30.52	44.49	39.45	41.97
MPTI [10]	39.27	36.14	37.71	46.90	43.59	45.25	29.96	27.26	28.61	38.14	34.36	36.25
AttMPTI [10]	42.55	40.83	41.69	54.00	50.32	52.16	35.23	30.72	32.98	46.74	40.80	43.77
Aug-FT-P [38]	48.49	43.06	45.78	58.97	54.35	56.66	38.49	35.07	36.78	50.95	45.69	48.32
Aug-FT-A [38]	42.89	40.78	41.84	54.35	51.39	52.87	35.47	30.55	33.01	47.11	41.80	44.46
CWT [54]	42.33	41.78	42.05	55.60	53.77	56.48	-	-	-	-	-	-
BFG [55]	42.15	40.52	41.34	51.23	49.39	50.31	34.12	31.98	33.05	46.25	41.38	43.82
SCAT [41]	54.92	56.74	55.83	64.24	69.03	66.63	-	-	-	-	-	-
PEFC [42]	45.31	44.86	45.09	56.26	54.06	55.16	38.78	36.13	37.46	51.72	46.05	48.89
PAPFZS3D [11]	57.08	55.94	56.51	64.55	59.64	62.10	55.27	55.60	55.44	59.02	53.16	56.09
2CBR [12]	50.73	47.66	49.20	52.35	47.14	49.75	47.00	46.36	46.68	45.06	39.47	42.27
Seg-PN [40]	63.15	64.32	63.74	67.08	**69.05**	68.07	61.80	**65.34**	63.57	62.94	**68.26**	65.60
Ours	**65.21**	**65.18**	**65.19**	**68.20**	68.49	**68.35**	**63.30**	63.86	**63.83**	**65.04**	66.27	**65.66**
FT [53]	47.97	44.89	46.45	59.86	54.27	57.12	38.70	32.07	35.46	51.77	43.87	47.93
ProtoNet [9]	50.66	47.27	48.99	62.39	59.16	60.80	44.32	41.43	42.89	54.40	51.83	53.12
AttProtoNet [9]	55.06	51.49	53.30	68.58	63.84	66.26	48.58	44.91	46.77	61.58	56.58	59.13
MPTI [10]	56.39	53.09	54.77	63.85	60.71	62.31	46.11	42.84	44.49	55.22	51.15	53.21
AttMPTI [10]	59.70	57.98	58.85	70.13	66.95	68.56	52.10	47.00	49.60	63.70	57.95	60.89
Aug-FT-P [38]	65.31	60.20	62.81	74.19	70.42	72.33	55.59	51.93	53.78	67.51	62.72	65.16
Aug-FT-A [38]	60.03	57.93	59.00	70.42	67.89	69.17	52.37	46.80	49.64	64.05	58.96	61.55
CWT [54]	59.48	58.94	59.20	71.47	69.94	72.19	-	-	-	-	-	-
BFG [55]	59.30	57.67	58.50	67.75	66.12	66.94	50.88	48.46	49.68	63.25	58.54	60.94
SCAT [41]	70.90	72.40	71.66	78.23	81.68	79.97	-	-	-	-	-	-
PEFC [42]	62.36	61.94	62.15	72.01	70.18	71.10	55.89	53.08	54.50	68.18	63.06	65.67
PAPFZS3D [11]	72.68	71.75	72.21	78.46	74.72	76.62	71.19	71.47	71.33	74.23	69.42	71.87
2CBR [12]	67.31	64.55	65.95	68.72	64.08	66.44	63.95	63.35	63.65	62.13	56.60	59.42
Seg-PN [40]	77.41	78.29	77.86	80.30	**81.69**	81.00	76.39	**79.04**	77.73	77.26	**81.14**	79.23
Ours	**78.94**	**78.92**	**78.93**	**81.09**	81.30	**81.20**	**77.53**	77.94	**77.92**	**78.82**	79.71	**79.27**

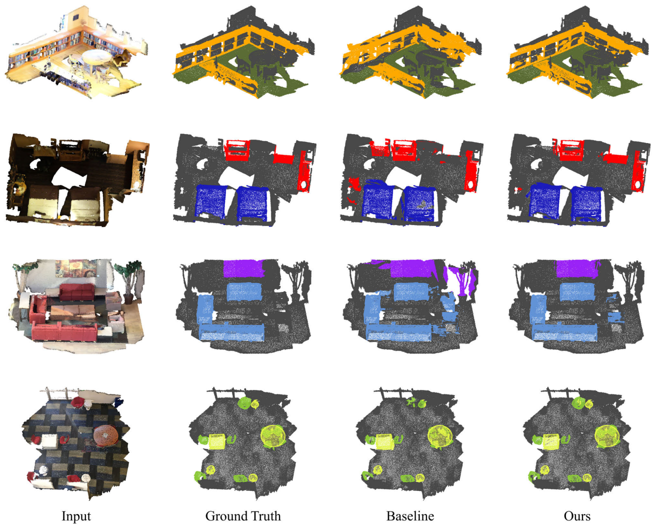

Fig. 5. Visualization of 2-way 1-shot segmentation result on *ScanNet* dataset. The involved classes are Bookshelf and Floor (first row), Cabinet and Bed (second row), Picture and Sofa (third row), and Table and Chair (last row); the background points are denoted by dark gray points.

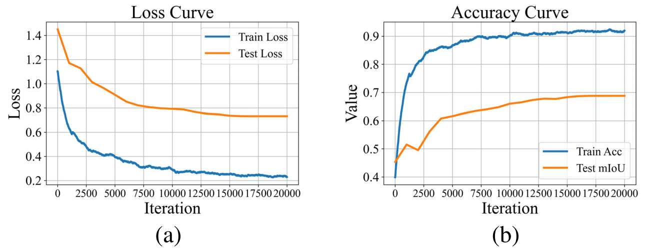

Fig. 6. Visualized (a) loss curve during training and testing, and (b) training accuracy curve and testing m-IoU curve for SDSimPoint. The testing process is conducted every 1000 iterations.

significant improvements in all methods. It has been noticed that the difficulty level of 3-way segmentation is higher than that of 2-way segmentation, which results in its generally lower performance. However, compared to other models, our method has a lower performance when changing the task from 2-way to 3-way. Such an improvement can be attributed to the "similarity-drive" learning of our method. Since the similarity between queries and prototypes has already been captured effectively during the forward process, we can directly predict the affiliation of each query point rather than constructing a graph with individual features [10] for prediction, which is easier to be influenced by noise. This not only proved the robustness of our method but also illustrated the similarity-based learning framework is effective for the few-shot semantic segmentation task.

2) Same-Domain Cross Pretraining: Tables III and IV illustrate the "cross pretraining" results, which means using one of the S3DIS and ScanNet datasets for pretraining and utilizing the other for training. These settings are more

TABLE III
S3DIS SEMANTIC SEGMENTATION RESULT USING SCANNET FOR PRETRAINING

Method	2-way						3-way					
	1-shot			5-shot			1-shot			5-shot		
	S^0	S^1	mean	S^0	S^1	mean	S^0	S^1	mean	S^0	S^1	mean
FT [53]	37.05	38.33	37.69	51.82	50.01	50.92	31.62	31.99	31.81	43.84	47.50	45.67
ProtoNet [9]	44.71	48.80	46.76	50.06	52.59	51.33	40.03	41.38	40.71	44.64	48.62	46.62
AttProtoNet [9]	49.96	50.01	49.99	53.35	55.61	54.48	37.28	44.69	40.99	42.33	52.35	47.34
MPTI [10]	48.27	47.56	47.92	55.21	52.56	53.89	36.80	37.71	37.23	39.09	41.73	40.41
AttMPTI [10]	51.14	48.90	50.02	57.80	62.61	60.20	39.80	42.06	40.93	43.25	51.68	47.47
PAPFZS3D [11]	58.65	64.91	61.78	64.72	69.33	67.03	48.52	56.05	52.29	61.11	59.54	60.33
Ours	**65.52**	**67.95**	**66.74**	**69.80**	**71.61**	**70.70**	**61.59**	**61.73**	**61.65**	**63.30**	**67.91**	**65.61**

TABLE IV
SCANNET SEMANTIC SEGMENTATION RESULT USING S3DIS FOR PRETRAINING

Method	2-way						3-way					
	1-shot			5-shot			1-shot			5-shot		
	S^0	S^1	mean	S^0	S^1	mean	S^0	S^1	mean	S^0	S^1	mean
FT [53]	28.45	29.72	29.09	30.69	34.28	32.49	24.70	19.40	22.05	32.81	29.58	31.20
ProtoNet [9]	36.98	34.04	36.00	40.79	40.21	40.50	30.65	28.17	29.41	33.70	36.00	34.85
AttProtoNet [9]	37.04	33.85	35.45	47.30	41.82	44.56	32.00	28.45	30.23	39.71	35.40	37.56
MPTI [10]	35.81	33.69	34.75	42.67	38.11	40.39	30.53	27.49	29.01	33.80	31.94	32.87
AttMPTI [10]	35.36	34.28	34.82	45.19	38.80	42.00	28.96	25.33	27.15	35.14	30.96	33.05
PAPFZS3D [11]	56.37	55.05	55.71	62.80	59.33	61.07	52.41	53.72	53.06	58.10	52.57	55.34
Ours	**64.37**	**64.58**	**64.48**	**65.46**	**66.08**	**65.77**	**60.96**	**62.33**	**61.65**	**63.62**	**65.36**	**64.49**

TABLE V
SEMANTIC SEGMENTATION RESULT USING SHAPENETPART FOR PRETRAINING

Dataset	Method	2-way						3-way					
		1-shot			5-shot			1-shot			5-shot		
		S^0	S^1	mean	S^0	S^1	mean	S^0	S^1	mean	S^0	S^1	mean
S3DIS	FT [53]	25.33	30.60	27.97	30.92	36.19	33.56	15.05	20.68	17.87	18.89	21.09	19.99
	ProtoNet [9]	39.16	39.00	39.08	45.72	47.39	46.56	30.84	32.11	31.48	40.23	41.70	40.97
	AttProtoNet [9]	42.25	39.70	40.98	51.48	51.71	51.60	35.62	36.10	35.86	42.50	43.54	43.02
	MPTI [10]	40.12	41.53	40.83	45.80	46.97	46.39	32.04	31.66	31.85	39.54	40.10	39.82
	AttMPTI [10]	43.45	44.91	44.18	49.77	53.81	51.79	33.90	32.11	33.01	46.94	43.90	45.42
	PAPFZS3D [11]	52.90	57.36	55.13	60.27	63.15	61.71	46.36	55.70	51.03	55.82	56.43	56.13
	Ours	**60.93**	**65.17**	**63.05**	**64.37**	**66.06**	**65.22**	**61.25**	**63.53**	**62.39**	**61.43**	**64.49**	**62.96**
ScanNet	FT [53]	12.39	12.04	12.22	13.57	13.02	13.30	8.56	9.43	9.00	10.17	11.48	10.83
	ProtoNet [9]	22.16	18.52	20.34	37.98	39.05	38.52	17.44	16.31	16.88	32.69	30.12	31.41
	AttProtoNet [9]	27.43	19.97	23.70	39.60	40.17	39.89	19.95	18.84	19.40	35.89	35.00	35.45
	MPTI [10]	20.78	19.53	20.16	39.85	39.02	39.44	16.26	19.48	17.87	32.72	29.91	31.32
	AttMPTI [10]	22.45	21.61	22.03	40.03	39.80	39.92	17.35	18.58	17.97	33.25	30.37	31.81
	PAPFZS3D [11]	49.28	50.14	49.71	52.06	52.50	52.28	45.83	44.79	45.31	49.46	48.08	48.77
	Ours	**54.94**	**53.20**	**54.07**	**55.39**	**54.25**	**55.30**	**50.47**	**50.75**	**50.61**	**51.19**	**52.38**	**51.79**

practical because, in real-world semantic segmentation tasks, it is almost impossible for us to find the same annotated dataset to pretrain our model, while we can utilize a public dataset from the same domain to pretrain our model. We can tell from the tables that all the models have decreased performance compared to the same-domain same pretraining settings. This is because of the distribution shift between datasets. Although our model performs slightly worse in this scenario, it still outperforms other baselines, which indicates the superiority of our SDSimPoint in such a situation.

3) Cross-Domain Cross Pretraining: Additionally, we argue that since our method emphasizes similarity rather than specific class affiliation, it is possible to use datasets from other domains for pretraining as long as our feature extractor can learn the similarity. Therefore, we explore the performance of our method with ShapeNetPart [63], a widely adopted dataset for part segmentation tasks, which encompasses 16 846 point clouds across 50 semantic classes. Given that the ShapeNetPart dataset includes some objects that are also present in indoor scanning scenes, such as chairs, tables, and laptops, we propose the feasibility of pretraining our feature extractor on ShapeNetPart and subsequently training our model on S3DIS and ScanNet datasets, respectively. Table V presents the segmentation results. As shown in Table V, while the results are lower than those achieved by models pretrained with datasets in

TABLE VI
MODEL COMPLEXITY AND INFERENCE TIME

ID	Model	#Params.	Flops	Time (sec/block)
I	AttMPTI [10]	352.19K	7.12G	0.46
II	CWT [54]	685.64k	8.16G	-
III	PAPFZS3D [11]	2.48M	7.48G	0.53
IV	Ours	2.76M	8.37G	0.61

TABLE VII
ABLATION STUDY ON S3DIS S^0 WITH 2-WAY 1-SHOT

ID	BEAM	SA	DSM	SSM	Deep Fusion	Result
I						52.27
II		✓				53.77
III	✓					57.86
IV			✓			56.97
V			✓		✓	59.70
VI				✓		55.93
VII			✓	✓	✓	61.45
VIII		✓	✓			60.73
IX		✓	✓		✓	62.35
X		✓		✓		54.64
XI		✓	✓	✓	✓	62.65
XII	✓		✓			63.18
XIII	✓		✓		✓	65.35
XIV	✓			✓		64.49
XV	✓		✓	✓	✓	**68.73**

the same domain (in-door scanning point clouds), our model outperforms the baseline models in these specific settings in terms of segmentation performance. Table VI illustrates the complexity and inference time of our model with the comparison of other methods. Due to our SSM and DSM being based on transformer structures, the parameters amount, the FLOPs, and the cost of time are larger than others, but these are acceptable scarification considering the improvement of performance.

D. Ablation Study

We initiate the ablation studies by conducting experiments on the S3DIS dataset to evaluate the effectiveness of different components within our SDSimPoint. Given the frequent use of attention-based blocks in our SSM and DSM, we delve deeper into the study of their dropout rates and normalization methods. To substantiate the advantage of our BEAM, we also compare its performance against other popular attention forms. Finally, we argue that the structure of the SSM can be flexible as long as it can capture sufficient shallow similarity. As such, we undertake experiments using SSMs with varying structures.

1) Model Components: To investigate the effectiveness of each component in our method, different settings of our model are selected. The BEAM block and the SA block will not be adopted at the same time since they share the same function. The deep fusion mechanism is not available when the DSM is not utilized. Based on these preconditions, an ablation study is conducted, and the results are shown in Table VII. Experiment I shows the result when disabling all modules of our network with the final prediction process is conducted as attMPTI [10]. Experiment II illustrates the performance when adding an SA for further feature refinement. As discussed in Section III-C, the BEAM has better learning ability on the dataset scale. Experiment III tells that it can lead to a notable improvement if we adopt BEAM rather than SA. Experiments IV and VI illustrate the effectiveness of the DSM and SSM, and they outperform the attMPTI without any help of attention mechanism. Experiment V indicates the importance of deep fusion, and it helps the DSM to better capture the similarity between the query samples and support samples.

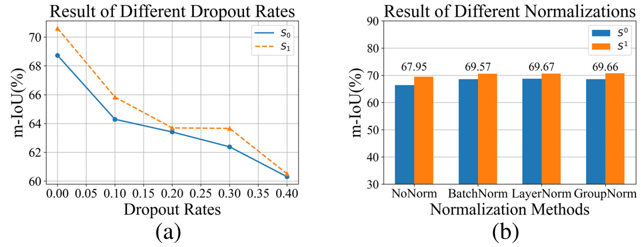

Fig. 7. Effectiveness of (a) different dropout rates and (b) different normalization methods on the S3DIS dataset with 2-way 1-shot. The blue line and blue bars denote the split 0, and the orange dashed line and orange bars denote the split 1. The numbers above the colored bar represent the mean value of the corresponding experimental group.

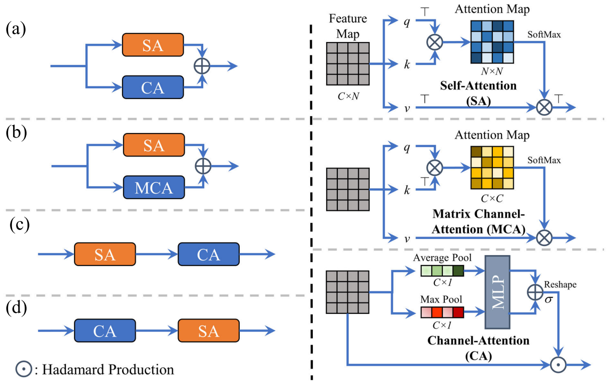

Fig. 8. Structure of different attention modules (a) and (b): additive (c) and (d): sequential. CA represents the channel attention, SA is the self-attention, and MCA indicates the matrix channel attention. ⊤ in the figure is the matrix transportation, and σ is the Sigmoid function.

2) Dropout Rates and Normalization Methods: Fig. 7 illustrates the results of different settings on dropout rates and normalization methods. Fig. 7(a) indicates that with the increase in the dropout rate, the segmentation performance will be worse. This is because the data are relatively scarce in few-shot learning tasks; if the model has a large dropout rate, it is difficult for it to learn sufficient knowledge. From Fig. 7(b), we can tell that there is no huge difference between models with various normalization methods, and all of them are better than the model without any normalization method.

3) Attention Modules: To additionally verify the advantage of our BEAM, Fig. 8 illustrates some famous attention mechanisms including the dual attention [64], CBAM [65], and their combinations. We substitute our BEAM with an attention module whose form is shown in Fig. 8(a)–(d), respectively, and then conduct experiments on S3DIS with a 2-way 1-shot few-shot setting.

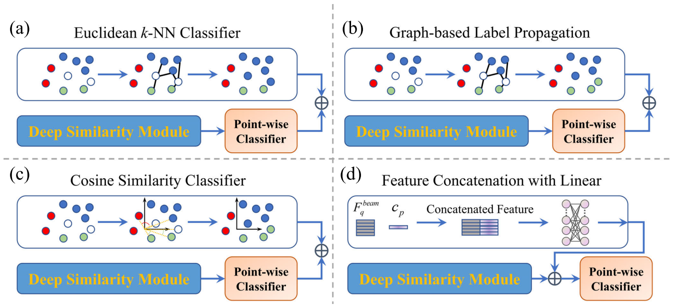
(a)
Euclidean k-NN Classifier
(b)
Graph-based Label Propagation
Deep Similarity Module
Point-wise Classifier
(c)
Cosine Similarity Classifier
(d)
Feature Concatenation with Linear
F_q^{beam}
c_p
Concatenated Feature

Fig. 9. Visualization of various forms of the SSM (a) Euclidean-based k-NN classifier, (b) label propagation, (c) cosine similarity-based classifier, and (d) linear layer. The blue, red, and green circles represent prototypes of three different classes, while the unfilled circles represent query features awaiting labeling.

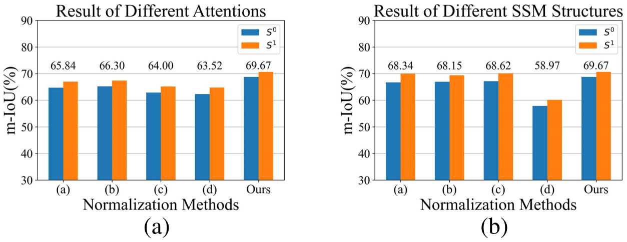

Fig. 10. Ablation studies for (a) attention modules and (b) SSM structures on S3DIS with 2-way 1-shot setting. The numbers above the colored bar represent the mean value of the corresponding experiment group.

4) SSM Structures: Fig. 9(a)–(d) illustrates the possible forms of the SSM, and the Euclidean k-NN classifier computes the k-nearest neighbors of the query sample and directly assigns the label of the class with most neighbors and the minimal average distance. The graph-base label propagation first constructs a graph with the query sample and its k-nearest neighbors, and then applies the label propagation algorithm [66] to obtain the possibility for classification. The feature concatenation concatenates the query feature with the prototype feature of each class and then adopts a linear layer to obtain the similarity. Since some nonparametric algorithms in Fig. 9 directly output the one-hot prediction vector, we add the vector with the output from the pointwise classifier that deals with the features from DSM, and then adopt an extra SoftMax operation to get the final prediction. Fig. 10(a) depicts the result comparison of different attention modules. The histogram shows that our BEAM excels other popular attention modules. Fig. 10(b) indicates the result of SSM with different structures; the numerical result illustrates that a nonparametric SSM can also perform well in our framework while the rough feature concatenation is not able to learn the shallow similarity well.

5) Noise Intensity: To investigate the influence of augmentation intensity during testing, we categorize the noises into the following types: 1) scaling: scaling the point cloud with a certain number and 2) jittering: adding Gaussian noise to each point. We vary the scaling factor from 0.1 to 3 and change the Gaussian noise's mean and derivation. Fig. 11(a) illustrates the result with different scaling factors. We can see that too small or too large scaling leads to decreased performance. This is because the scaled point cloud might confuse our model when grasping the global semantic information. Fig. 11(b) shows the performance under different intensities of noise. It can be concluded that with a larger derivation, the performance will decrease more. Compared to the baseline, our method is more robust, facing the change of mean.

TABLE VIII

Model Performance Under Different Hyperparameter Settings on S3DIS S^0 in 2-Way 1-Shot

Hyperparameter	Value	mIoU
Learning rate	5e-4, 1e-3, 5e-3	67.64, 68.73, 66.96
Decoder block number	2, 3, 4	68.50, 68.73, 68.76
Backbone k-NN number	10, 20, 30	67.41, 68.73, 68.82
Augmentation epochs	50, 60, 70	68.61, 68.73, 68.55
Pre-train batch size	8, 16, 32	67.22, 68.73, 68.81
EMA weight α	0.9, 0.99, 0.999	68.50, 68.73, 68.49
Prototype numbers	50, 100, 150	67.08, 68.73, 68.30

TABLE IX

Ablation Study of Different Distance Metrics on S3DIS Dataset

Distance Metric	2-way 1-shot			3-way 1-shot		
	S^0	S^1	mean	S^0	S^1	mean
Euclidean	44.18	42.53	43.34	39.71	40.83	40.27
Cosine	56.42	55.07	55.75	51.61	51.49	51.55
Ours	**68.73**	**70.61**	**69.67**	**62.28**	**62.11**	**62.19**

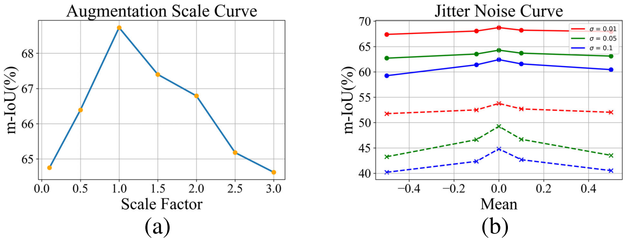

Fig. 11. Ablation study for different intensities of (a) scaling augmentation and (b) Gaussian jitter noise. The solid line in (b) denotes our method, while the dashed line in (b) represents the baseline.

6) Hyperparameters Analysis: Table VIII illustrates the influence of different hyperparameter settings. A too-large or too-small learning rate will downgrade the model's performance due to an inappropriate gradient. Although more decoder blocks may improve the performance, it requires more training resources and suffers from the risk of overfitting. The k-NN number of the backbone controls the "receptive field," with a larger number, the model can grab more information, but the inference and training speed will be significantly slow down. The augmentation epochs of the dynamic augmentor during pretraining control the diversity of augmentation patterns, more epochs will bring more augmentation strategies but confuse the backbone, and fewer epochs might not be enough to learn a robust representation. The weight factor of the EMA process in BEAM and the prototype numbers influence the quality of features, which implicitly affect the captured similarity. With relative experiments, we find that 0.99 and 100 are suitable values considering both accuracy and efficiency.

7) Distance Metric: To investigate the influence of different distance metrics, we compare two distance functions with our learnable metric: the Euclidean distance and the cosine similarity. Table IX illustrates the comparison result. Since our features are fused with similarity, the nonparametric distance metric, like Euclidean distance, is not appropriate for prediction since it focuses on figuring out the distance between features rather than directly predicting affiliation from similarity. On the contrary, our learnable distance metric conducts pointwise classification from the similarity, which is more suitable for our framework.

V. Conclusion

In this work, we propose SDSimPoint, a noteworthy few-shot point cloud semantic segmentation network based on shallow–deep similarity learning. We design a BEAM that uses two memory units to replace the matrix multiplication in the attention mechanism, thus enabling the range of the attention map to expand from a single episode to the whole training dataset. We introduce an SSM and a DSM to capture both shallow and deep similarities. This helps our model to acquire sufficient information, even when pretrained in a class-agnostic self-supervision manner. A query-prototype deep fusion mechanism has been devised for DSM with the objective of facilitating interactions between the query feature and class prototypes, and thus allows for the fusion of query features with prototype information, ultimately enhancing prediction results. Comprehensive experiments are implemented to verify the effectiveness and robustness of the proposed method.

Acknowledgment

The authors would like to acknowledge valuable discussions with Dr. Hendrik Schafstall and Dr. Arno Zinke during their tenure previously at Hexagon, Manufacturing Intelligence Division, Simufact Engineering GmbH.

References

[1] Y. Li et al., "Deep learning for LiDAR point clouds in autonomous driving: A review," *IEEE Trans. Neural Netw. Learn. Syst.*, vol. 32, no. 8, pp. 3412–3432, Aug. 2021.

[2] C. R. Qi, H. Su, K. Mo, and L. J. Guibas, "PointNet: Deep learning on point sets for 3D classification and segmentation," in *Proc. IEEE Conf. Comput. Vis. Pattern Recognit. (CVPR)*, Jul. 2017, pp. 652–660.

[3] C. R. Qi, Y. Li, H. Su, and L. Guibas, "PointNet++: Deep hierarchical feature learning on point sets in a metric space," in *Proc. Adv. Neural Inf. Process. Syst. (NeruIPS)*, Jan. 2017, pp. 1–20.

[4] S. Li, Y. Liu, and J. Gall, "Rethinking 3-D LiDAR point cloud segmentation," *IEEE Trans. Neural Netw. Learn. Syst.*, vol. 36, no. 3, pp. 4079–4090, 2025, doi: 10.1109/TNNLS.2021.3132836.

[5] Z. Du, H. Ye, and F. Cao, "A novel local–global graph convolutional method for point cloud semantic segmentation," *IEEE Trans. Neural Netw. Learn. Syst.*, vol. 35, no. 4, pp. 4798–4812, 2024, doi: 10.1109/TNNLS.2022.3155282.

[6] B. Liu, J. Jiao, and Q. Ye, "Harmonic feature activation for few-shot semantic segmentation," *IEEE Trans. Image Process.*, vol. 30, pp. 3142–3153, 2021.

[7] B. Yang, F. Wan, C. Liu, B. Li, X. Ji, and Q. Ye, "Part-based semantic transform for few-shot semantic segmentation," *IEEE Trans. Neural Netw. Learn. Syst.*, vol. 33, no. 12, pp. 7141–7152, Dec. 2022.

[8] H. Gao, J. Xiao, Y. Yin, T. Liu, and J. Shi, "A mutually supervised graph attention network for few-shot segmentation: The perspective of fully utilizing limited samples," *IEEE Trans. Neural Netw. Learn. Syst.*, vol. 35, no. 4, pp. 1–13, Aug. 2022.

[9] J. Wang and Y. Zhai, "Prototypical Siamese networks for few-shot learning," in *Proc. IEEE 10th Int. Conf. Electron. Inf. Emergency Commun. (ICEIEC)*, Jul. 2020, pp. 178–181.

[10] N. Zhao, T.-S. Chua, and G. H. Lee, "Few-shot 3D point cloud semantic segmentation," in *Proc. IEEE Conf. Comput. Vis. Pattern Recognit.*, Jun. 2021, pp. 8873–8882.

[11] S. He, X. Jiang, W. Jiang, and H. Ding, "Prototype adaption and projection for few- and zero-shot 3D point cloud semantic segmentation," *IEEE Trans. Image Process.*, vol. 32, pp. 3199–3211, 2023.

[12] G. Zhu, Y. Zhou, R. Yao, and H. Zhu, "Cross-class bias rectification for point cloud few-shot segmentation," *IEEE Trans. Multimedia*, vol. 25, pp. 9175–9188, 2023.

[13] Z. An et al., "Rethinking few-shot 3D point cloud semantic segmentation," in *Proc. IEEE/CVF Conf. Comput. Vis. Pattern Recognit. (CVPR)*, Jun. 2024, pp. 3996–4006.

[14] J. Wang, H. Zhu, H. Guo, A. A. Mamun, C. Xiang, and T. H. Lee, "Few-shot point cloud semantic segmentation via contrastive self-supervision and multi-resolution attention," in *Proc. IEEE Int. Conf. Robot. Autom. (ICRA)*, May 2023, pp. 2811–2817.

[15] Z. Li, Z. Hu, W. Luo, and X. Hu, "SaberNet: Self-attention based effective relation network for few-shot learning," *Pattern Recognit.*, vol. 133, Jan. 2023, Art. no. 109024.

[16] O. K. Shirekar, A. Singh, and H. Jamali-Rad, "Self-attention message passing for contrastive few-shot learning," in *Proc. IEEE/CVF Winter Conf. Appl. Comput. Vis. (WACV)*, Jan. 2023, pp. 5414–5425.

[17] Z. Chen, Y. Fu, K. Chen, and Y.-G. Jiang, "Image block augmentation for one-shot learning," in *Proc. AAAI Conf. Artif. Intell.*, 2019, pp. 3379–3386.

[18] L. Zhang et al., "What makes a good data augmentation for few-shot unsupervised image anomaly detection?" in *Proc. IEEE/CVF Conf. Comput. Vis. Pattern Recognit. Workshops (CVPRW)*, Jun. 2023, pp. 4345–4354.

[19] A. Santoro, S. Bartunov, M. Botvinick, D. Wierstra, and T. Lillicrap, "Meta-learning with memory-augmented neural networks," in *Proc. Int. Conf. Mach. Learn.*, Jun. 2016, pp. 1842–1850.

[20] N. Mishra, M. Rohaninejad, X. Chen, and P. Abbeel, "A simple neural attentive meta-learner," in *Proc. Int. Conf. Learn. Represent. (ICLR)*, Jan. 2017.

[21] S. Rahman, S. Khan, and F. Porikli, "A unified approach for conventional zero-shot, generalized zero-shot, and few-shot learning," *IEEE Trans. Image Process.*, vol. 27, no. 11, pp. 5652–5667, Nov. 2018.

[22] A. A. Rusu et al., "Meta-learning with latent embedding optimization," in *Proc. Int. Conf. Learn. Represent. (ICLR)*, Jan. 2019.

[23] A. Zhmoginov, M. Sandler, and M. Vladymyrov, "Hypertransformer: Model generation for supervised and semi-supervised few-shot learning," in *Proc. Int. Conf. Mach. Learn. (ICML)*, 2022, pp. 27075–27098.

[24] C. Finn, P. Abbeel, and S. Levine, "Model-agnostic meta-learning for fast adaptation of deep networks," in *Proc. 34th Int. Conf. Mach. Learn.*, vol. 70, Aug. 2017, pp. 1126–1135.

[25] Z. Ji, Z. Hou, X. Liu, Y. Pang, and J. Han, "Information symmetry matters: A modal-alternating propagation network for few-shot learning," *IEEE Trans. Image Process.*, vol. 31, pp. 1520–1531, 2022.

[26] B. Xi, J. Li, Y. Li, R. Song, D. Hong, and J. Chanussot, "Few-shot learning with class-covariance metric for hyperspectral image classification," *IEEE Trans. Image Process.*, vol. 31, pp. 5079–5092, 2022.

[27] J. Zhou, Y. Zheng, J. Tang, L. Jian, and Z. Yang, "FlipDA: Effective and robust data augmentation for few-shot learning," in *Proc. 60th Annu. Meeting Assoc. Comput. Linguistics*, 2022, pp. 8646–8665.

[28] Y. He et al., "Learning better registration to learn better few-shot medical image segmentation: Authenticity, diversity, and robustness," *IEEE Trans. Neural Netw. Learn. Syst.*, vol. 35, no. 2, pp. 2588–2601, Feb. 2024.

[29] H. Cheng, Y. Wang, H. Li, A. C. Kot, and B. Wen, "Disentangled feature representation for few-shot image classification," *IEEE Trans. Neural Netw. Learn. Syst.*, vol. 35, no. 8, pp. 10422–10435, Aug. 2024.

[30] Z. Zhou et al., "Task-related saliency for few-shot image classification," *IEEE Trans. Neural Netw. Learn. Syst.*, vol. 35, no. 8, pp. 10751–10763, Aug. 2024.

[31] Y. Liu, L. Zhu, X. Wang, M. Yamada, and Y. Yang, "Bilaterally normalized scale-consistent sinkhorn distance for few-shot image classification," *IEEE Trans. Neural Netw. Learn. Syst.*, vol. 35, no. 8, pp. 11475–11485, Aug. 2024.

[32] L. Landrieu and M. Simonovsky, "Large-scale point cloud semantic segmentation with superpoint graphs," in *Proc. IEEE/CVF Conf. Comput. Vis. Pattern Recognit.*, Jun. 2018, pp. 4558–4567.

[33] X. Ma, C. Qin, H. You, H. Ran, and Y. Fu, "Rethinking network design and local geometry in point cloud: A simple residual MLP framework," in *Proc. Int. Conf. Learn. Represent. (ICLR)*, Jan. 2022.

[34] G. Qian et al., "PointNeXt: Revisiting PointNet++ with improved training and scaling strategies," in *Proc. Adv. Neural Inf. Process. Syst.*, vol. 35, Jan. 2022, pp. 23192–23204.

[35] H. Zhao, L. Jiang, J. Jia, P. Torr, and V. Koltun, "Point transformer," in *Proc. IEEE/CVF Int. Conf. Comput. Vis. (ICCV)*, Oct. 2021, pp. 16259–16268.

[36] X. Lai et al., "Stratified transformer for 3D point cloud segmentation," in *Proc. IEEE/CVF Conf. Comput. Vis. Pattern Recognit. (CVPR)*, Jun. 2022, pp. 8500–8509.

[37] X. Wu et al., "Point transformer v3: Simpler, faster, stronger," 2023, *arXiv:2312.10035*.

[38] L. Lai, J. Chen, C. Zhang, Z. Zhang, G. Lin, and Q. Wu, "Tackling background ambiguities in multi-class few-shot point cloud semantic segmentation," *Knowl.-Based Syst.*, vol. 253, Oct. 2022, Art. no. 109508.

[39] G. Zhang, G. Kang, Y. Yang, and Y. Wei, "Few-shot segmentation via cycle-consistent transformer," in *Proc. NIPS*, vol. 34, 2021, pp. 21984–21996.

[40] X. Zhu et al., "No time to train: Empowering non-parametric networks for few-shot 3D scene segmentation," in *Proc. IEEE/CVF Conf. Comput. Vis. Pattern Recognit. (CVPR)*, Jun. 2024, pp. 3838–3847.

[41] C. Zhang, Z. Wu, X. Wu, Z. Zhao, and S. Wang, "Few-shot 3D point cloud semantic segmentation via stratified class-specific attention based transformer network," in *Proc. AAAI Conf. Artif. Intell.*, vol. 37, Jun. 2023, pp. 3410–3417.

[42] Q. Zhang, T. Wang, F. Hao, F. Wu, and J. Cheng, "Prototype expansion and feature calibration for few-shot point cloud semantic segmentation," *Neurocomputing*, vol. 558, Nov. 2023, Art. no. 126732.

[43] J. Wang, H. Zhu, H. Guo, A. Al Mamun, P. Vadakkepat, and T. H. Lee, "CAM/CAD point cloud part segmentation via few-shot learning," in *Proc. IEEE 20th Int. Conf. Ind. Informat. (INDIN)*, Jul. 2022, pp. 359–365.

[44] J. Wang, H. Zhu, H. Guo, A. Al Mamun, C. W. De Silva, and T. H. Lee, "Few-shot point cloud semantic segmentation for CAM/CAD via feature enhancement and efficient dual attention," in *Proc. 49th Annu. Conf. IEEE Ind. Electron. Soc.*, Oct. 2023, pp. 1–6.

[45] A. Dosovitskiy et al., "An image is worth 16×16 words: Transformers for image recognition at scale," in *Proc. Int. Conf. Learn. Represent. (ICLR)*, Jan. 2020.

[46] H. Zhao, J. Jia, and V. Koltun, "Exploring self-attention for image recognition," in *Proc. IEEE/CVF Conf. Comput. Vis. Pattern Recognit. (CVPR)*, Jun. 2020, pp. 10076–10085.

[47] M. Guo, Z. Liu, T. Mu, and S. Hu, "Beyond self-attention: External attention using two linear layers for visual tasks," *IEEE Trans. Pattern Anal. Mach. Intell.*, vol. 45, no. 5, pp. 5436–5447, May 2023.

[48] L. Wang, X. Li, and Y. Fang, "Few-shot learning of part-specific probability space for 3D shape segmentation," in *Proc. IEEE/CVF Conf. Comput. Vis. Pattern Recognit. (CVPR)*, Jun. 2020, pp. 4503–4512.

[49] V. G. Satorras and J. B. Estrach, "Few-shot learning with graph neural networks," in *Proc. Int. Conf. Learn. Represent. (ICLR)*, Feb. 2018.

[50] L. H. Li et al., "Grounded language-image pre-training," in *Proc. IEEE/CVF Conf. Comput. Vis. Pattern Recognit.*, Jun. 2022, pp. 10965–10975.

[51] H. Zhang et al., "GLIPv2: Unifying localization and vision-language understanding," in *Proc. Adv. Neural Inf. Process. Syst. (NeurIPS)*, Jan. 2022, pp. 36067–36080.

[52] Z.-Y. Dou et al., "Coarse-to-fine vision-language pre-training with fusion in the backbone," in *Proc. Adv. Neural Inf. Process. Syst. (NeurIPS)*, vol. 35, 2022, pp. 32942–32956.

[53] A. Shaban, S. Bansal, Z. Liu, I. Essa, and B. Boots, "One-shot learning for semantic segmentation," in *Proc. Brit. Mach. Vis. Conf.*, Sep. 2017, pp. 167.1–167.13.

[54] Z. Lu, S. He, X. Zhu, L. Zhang, Y.-Z. Song, and T. Xiang, "Simpler is better: Few-shot semantic segmentation with classifier weight transformer," in *Proc. IEEE/CVF Int. Conf. Comput. Vis. (ICCV)*, Oct. 2021, pp. 8741–8750.

[55] Y. Mao, Z. Guo, X. Lu, Z. Yuan, and H. Guo, "Bidirectional feature globalization for few-shot semantic segmentation of 3D point cloud scenes," in *Proc. Int. Conf. 3D Vis. (3DV)*, Sep. 2022, pp. 505–514.

[56] I. Armeni, S. Sax, A. R. Zamir, and S. Savarese, "Joint 2D–3D-semantic data for indoor scene understanding," 2017, *arXiv:1702.01105*.

[57] A. Dai, A. X. Chang, M. Savva, M. Halber, T. Funkhouser, and M. Nießner, "ScanNet: Richly-annotated 3D reconstructions of indoor scenes," in *Proc. IEEE Conf. Comput. Vis. Pattern Recognit. (CVPR)*, Jul. 2017, pp. 2432–2443.

[58] Y. Wang, Y. Sun, Z. Liu, S. E. Sarma, M. M. Bronstein, and J. M. Solomon, "Dynamic graph CNN for learning on point clouds," *ACM Trans. Graph.*, vol. 38, no. 5, pp. 1–12, 2019.

[59] T. Wu, L. Pan, J. Zhang, T. Wang, Z. Liu, and D. Lin, "Density-aware chamfer distance as a comprehensive metric for point cloud completion," in *Proc. Adv. Neural Inf. Process. Syst. (NeurIPS)*, Jan. 2021, pp. 29088–29100.

[60] J. L. Ba, J. R. Kiros, and G. E. Hinton, "Layer normalization," *Stat*, vol. 1050, p. 21, Jul. 2016.

[61] A. Newell and J. Deng, "How useful is self-supervised pretraining for visual tasks?" in *Proc. IEEE/CVF Conf. Comput. Vis. Pattern Recognit. (CVPR)*, Jun. 2020, pp. 7343–7352.

[62] M. Wang and W. Deng, "Deep visual domain adaptation: A survey," *Neurocomputing*, vol. 312, pp. 135–153, Oct. 2018.

[63] L. Yi et al., "A scalable active framework for region annotation in 3D shape collections," *ACM Trans. Graph. (ToG)*, vol. 35, no. 6, pp. 1–12, 2016.

[64] J. Fu et al., "Dual attention network for scene segmentation," in *Proc. IEEE/CVF Conf. Comput. Vis. Pattern Recognit. (CVPR)*, Jun. 2019, pp. 3141–3149.

[65] S. Woo, J. Park, J.-Y. Lee, and I. S. Kweon, "CBAM: Convolutional block attention module," in *Proc. Eur. Conf. Comput. Vis.*, Sep. 2018, pp. 3–19.

[66] A. Iscen, G. Tolias, Y. Avrithis, and O. Chum, "Label propagation for deep semi-supervised learning," in *Proc. IEEE/CVF Conf. Comput. Vis. Pattern Recognit. (CVPR)*, Jun. 2019, pp. 5065–5074.

Jiahui Wang received the B.S. degree in opto-electronic information science and engineering from the School of Physics, Harbin Institute of Technology, Harbin, China, in 2020. He is currently pursuing the Ph.D. degree with the Department of Electrical and Computer Engineering, National University of Singapore, Singapore.

His current research interests include point cloud understanding, 3-D computer vision, and AI application with robotics.

Haiyue Zhu (Member, IEEE) received the B.Eng. degree in automation from the School of Electrical Engineering and Automation, Tianjin University, Tianjin, China, in 2010, the B.Mgt. degree in business administration from the College of Management and Economics, Tianjin University, in 2010, and the M.Sc. and Ph.D. degrees in electrical engineering from the National University of Singapore, Singapore, in 2013 and 2017, respectively.

He is currently a Senior Scientist with the Adaptive Robotics and Mechatronics Group, Singapore Institute of Manufacturing Technology (SIMTech), Agency for Science, Technology and Research (A*STAR), Singapore. His current research interests include intelligent robotics systems, vision and perception, and artificial intelligence.

Haoren Guo received the B.Eng. degree in electrical engineering from the National University of Singapore, Singapore, in 2021, where she is currently pursuing the Ph.D. degree with the Department of Electrical and Computer Engineering.

Her current research interests include time-series forecasting, machinery predictive maintenance, and domain adaptation.

Abdullah Al Mamun received the B.Tech. degree (Hons.) in electronics and electrical communication engineering from IIT Kharagpur, Kharagpur, India, in 1985, and the Ph.D. degree in electrical engineering from the National University of Singapore (NUS), Singapore, in 1997.

He is currently an Associate Professor with NUS. His research interests include precision mechatronics, servomechanism in data storage devices, intelligent control, and mobile robots.

Cheng Xiang (Member, IEEE) received the B.S. degree from Fudan University, Shanghai, China, in 1991, the M.S. degree from the Institute of Mechanics, Chinese Academy of Sciences, Beijing, China, in 1994, and the M.S. and Ph.D. degrees in electrical engineering from Yale University, New Haven, CT, USA, in 1995 and 2000, respectively.

He is currently an Associate Professor and the Area Director of control, intelligent systems and robotics with the Department of Electrical and Computer Engineering, National University of Singapore, Singapore. His research interests include computational intelligence, adaptive systems, and pattern recognition.

Clarence W. de Silva (Life Fellow, IEEE) received the first Ph.D. degree in mechanical engineering from Massachusetts Institute of Technology, Cambridge, MA, USA, in 1978, the second Ph.D. degree in information engineering from the University of Cambridge, Cambridge, U.K., in 1998, the Honorary D.Eng. degree from the University of Waterloo, Waterloo, ON, Canada, in 2008, and the Higher Doctorate (Sc.D.) degree in mechatronics and automation from the University of Cambridge, in 2020.

He has been a Professor of mechanical engineering with The University of British Columbia, Vancouver, BC, Canada, since 1988. His appointments include the Tier 1 Canada Research Chair of mechatronics and industrial automation, a Professorial Fellow, a Peter Wall Scholar, a Mobil Endowed Chair Professor, and the NSERCBC Packers Chair of industrial automation.

Dr. Silva is a fellow of ASME, the Canadian Academy of Engineering, and the Royal Society of Canada.

Tong Heng Lee received the B.A. degree (Hons.) in engineering tripos from Cambridge University, Cambridge, U.K., in 1980, the M.Eng. degree from the National University of Singapore (NUS), Singapore, in 1985, and the Ph.D. degree from Yale University, New Haven, CT, USA, in 1987.

He was a Past Vice-President (Research) of NUS. He is currently a Professor with the Department of Electrical and Computer Engineering, NUS, and also a Professor with the NUS Graduate School, NUS NGS (ISEP).